Aerospace Science and Technology 92 (2019) 958–971

Contents lists available at ScienceDirect

Aerospace Science and Technology

www.elsevier.com/locate/aescte

Implicit high-order gas kinetic scheme for turbulence simulation

Guiyu Cao [a], Hongmin Su [b], Jinxiu Xu [c], Kun Xu [a,d,*]

[a] Department of Mathematics, Department of Mechanical and Aerospace Engineering, Hong Kong University of Science and Technology, Clear Water Bay, Kowloon, Hong Kong
[b] National Key Laboratory of Science and Technology on Aerodynamic Design and Research, Northwestern Polytechnical University, Xi'an, Shaanxi 710072, China
[c] JiangNan Institute of Computing Technology, Wuxi, Jiangsu 214121, China
[d] HKUST Shenzhen Research Institute, Shenzhen 518057, China

ARTICLE INFO

Article history:
Received 3 April 2019
Received in revised form 7 June 2019
Accepted 5 July 2019
Available online 12 July 2019

Keywords:
Implicit high-order GKS
Two-stage fourth-order scheme
LU-SGS
Time-relaxation turbulence simulation

ABSTRACT

In recent years, coupled with traditional turbulence models, the second-order gas-kinetic scheme (GKS) has been used in the turbulent flow simulations. At the same time, high-order GKS has been developed, such as the two-stage fourth-order scheme (S2O4) GKS, and used for laminar flow calculations. In this paper, targeting on the high-Reynolds number engineering turbulent flows, an implicit high-order GKS with Lower-Upper Symmetric Gauss-Seidel (LU-SGS) technique is developed under the S2O4 framework. Based on Vreman-type LES model and $k-\omega$ SST model, a turbulent relaxation time is obtained and used for the determination of an enlarged particle collision time for the high-Reynolds number turbulent flow simulation. Numerical experiments include incompressible decaying homogeneous isotropic turbulence, incompressible high-Reynolds number flat plate turbulent flow, incompressible turbulence around NACA0012 airfoil, transonic turbulence around RAE2822 airfoil, and transonic high-Reynolds number ARA M100 wing-body simulation. Comparisons among the numerical solutions from current implicit high-order GKS, the explicit high-order GKS, the implicit second-order GKS, and experimental measurements have been conducted. Through these examples, it is concluded that the high-order GKS has high accuracy in space and time, especially for smooth flows, and obtains more accurate turbulent flow fields on coarse grids than the second-order GKS. In addition, significant acceleration on computational efficiency, as well as super robustness in simulating complex flows are confirmed from the current implicit high-order GKS. This study also indicates that turbulence modeling plays a dominant role in capturing physical solution, such as in the transonic three-dimensional complex RANS simulation, which is beyond the numerical discretization error, such as the differences between the second and fourth-order GKS.

1. Introduction

Turbulence is an important research subject among physics, applied mathematics, and engineering applications [1]. Because of its multi-scale features in space and time, it is a challenge to properly balance the accuracy requirements and computational costs [2] in the simulations, especially for high-Reynolds number turbulent flows. Currently, there are mainly four approaches for turbulence simulation, namely direct numerical simulation (DNS), large eddy simulation (LES), Reynolds averaged Navier-Stokes (RANS), and hybrid RANS/LES methods.

Theoretically, DNS [3–5] is supposed to resolve turbulent structures above the Kolmogrov dissipation scale [6] by grid and time step resolution, but the prohibitive cost limits DNS's engineering applications. In order to study turbulent flow on unresolved grids, such as for the high-Reynolds number turbulence problems, the RANS models [7–12], the LES models [13–16], and the hybrid RANS/LES methods [17–19] have been developed and applied. RANS captures turbulent structures above integral scale under the constraints of computational resources, which has been widely used in engineering turbulence simulations [20]. LES solves the filtered Navier-Stokes equations with resolvable turbulent structures above the inertial scale. Even though LES is quite expansive compared with RANS, for unsteady separation turbulent flows, LES has gradually become an indispensable tool to obtain high-resolution turbulent flow fields. To combine the advantages of RANS and LES, the hybrid RANS/LES methods have been proposed and become

* Corresponding author at: Department of Mathematics, Department of Mechanical and Aerospace Engineering, Hong Kong University of Science and Technology, Clear Water Bay, Kowloon, Hong Kong.
E-mail addresses: gcaoaa@connect.ust.hk (G. Cao), hongminsu@mail.nwpu.edu.cn (H. Su), jinxiu3186@sina.com (J. Xu), makxu@ust.hk (K. Xu).

https://doi.org/10.1016/j.ast.2019.07.020
1270-9638/

hot topics in turbulence simulations, which keep good balance between resolution accuracy and computational cost.

In the past decades, the second-order gas-kinetic scheme (GKS) [21,22] based on the Bhatnagar-Gross-Krook (BGK) [23] model has achieved great success for laminar flow computations from incompressible low-speed flow to hypersonic one. Different from the numerical methods based on the macroscopic governing equations, the gas-kinetic scheme presents a gas evolution process from kinetic scale to hydrodynamic scale, where both inviscid and viscous fluxes are recovered from the moments of a single time-dependent gas distribution function [21]. Additionally, both normal and tangential gradients of flow variables are included in the flux function across a cell interface [24]. It has been extended to flows with multi-temperature [25,26], gravitational field [27], and magneto-hydrodynamics [28]. For turbulent flows, GKS can be directly used as a DNS tool for low-Reynolds number flow [29,30]. The "mixing time" was proposed for kinetic equation based methods for high-Reynolds number turbulence [31,32], which can be regarded as an extension of BGK model with a newly defined collision (relaxation) time τ_t. Following this "mixing time" concept, the second-order gas kinetic schemes coupled with S-A model [33], $k-\omega$ SST model [34–36], Vreman-type LES model, and the hybrid RANS/LES methods [37] have been developed and implemented in high-Reynolds number turbulent flow simulations. Most previous work are based on the explicit second-order GKS coupled with traditional turbulence models. In view of the high-resolution requirement for turbulence simulation, it is fully legitimate to construct high-order GKS (HGKS) coupled with traditional turbulence models.

In recent years, an accurate and robust two-stage fourth-order (S2O4) GKS [38–40] has been developed for laminar flows, which achieves fourth-order accuracy in space and time and shows high efficiency and robustness in the flow simulations with shocks. More importantly, this scheme is as robust as the second-order scheme and works perfectly from the subsonic to the hypersonic viscous heat conducting flows [26]. The S2O4 GKS shows great potential in simulating turbulence accurately and robustly, especially for compressible turbulent flows. In this paper, focusing on the extension of the scheme to the three-dimensional turbulent flows, an implicit high-order GKS (IHGKS) is proposed in this paper. On the one hand, the S2O4 GKS framework is used to provide a solid foundation for obtaining high-resolution flow fields in turbulent flow. On the other hand, Lower-Upper Symmetric Gauss-Seidel (LU-SGS) method [41,42] is implemented to overcome the time step barrier in the explicit scheme, and makes the Courant-Friedrichs-Lewy (CFL) [43] number large in the three-dimensional high-Reynolds turbulent flows. In what follows, Section 2 presents the construction of this IHGKS under two-stage fourth-order framework. This is followed by the coupling of Vreman-type LES model [15] and the $k-\omega$ SST [10] model in current IHGKS in Section 3. The numerical simulations from incompressible low-speed to transonic three-dimensional complex turbulent flows will be presented in section 4. And the final section is the conclusion and discussion.

2. Implicit three-dimensional two-stage high-order GKS solver

2.1. Three-dimensional finite volume framework based on BGK model

Based on particle transport and collision, the Boltzmann equation has been constructed for monotonic dilute gas. The simplification of the Boltzmann equation given by the BGK model has the following form [23],

$$\frac{\partial f}{\partial t}+u\frac{\partial f}{\partial x}+v\frac{\partial f}{\partial y}+w\frac{\partial f}{\partial z}=\frac{g-f}{\tau}, \tag{1}$$

where f is the number density of molecules at position (x, y, z) and particle velocity (u, v, w) at time t. The left side of the Eq. (1) denotes the free transport term, and the right hand side represents the collision term. The relation between distribution function f and macroscopic variables, such as mass, momentum, energy, and stress, can be obtained by taking moments in velocity of the gas distribution function. The collision operator in BGK model shows simple relaxation process from f to a local equilibrium state g, with a characteristic time scale τ, which is related to the viscosity and heat conduction coefficients. The local equilibrium state is a Maxwellian distribution,

$$g=\rho(\frac{\lambda}{\pi})^{\frac{K+3}{2}}e^{-\lambda[(u-U)^2+(v-V)^2+(w-W)^2+\xi^2]}, \tag{2}$$

where ρ is the density, (U, V, W) are the macroscopic fluid velocity in the $x-$, $y-$ and $z-$ directions. Here $\lambda=m/2k_BT$, m is the molecular mass, k_B is the Boltzmann constant, and T is the temperature. For three-dimensional equilibrium diatomic gas, the total number of degrees of freedom in ξ is $K=2$, which accounts for the two rotational modes $\xi^2=\xi_1^2+\xi_2^2$, and the specific heat ratio $\gamma_s=(K+5)/(K+3)$ is determined.

The relation between mass ρ, momentum $(\rho U, \rho V, \rho W)$, total energy ρE with the distribution function f is given by,

$$Q=\begin{pmatrix}\rho\\ \rho U\\ \rho V\\ \rho W\\ \rho E\end{pmatrix}=\int\psi_\alpha f d\Xi,\quad \alpha=1,2,3,4,5, \tag{3}$$

where $d\Xi=dudvdwd\xi_1d\xi_2$ and ψ_α is the component of the vector of collision invariants

$$\begin{aligned}\psi&=(\psi_1,\psi_2,\psi_3,\psi_4,\psi_5)^T\\ &=(1,u,v,w,\frac{1}{2}(u^2+v^2+w^2+\xi^2))^T.\end{aligned}$$

Since only mass, momentum and total energy are conserved during particle collisions, the compatibility condition for the collision term turns into,

$$\int\frac{g-f}{\tau}\psi d\Xi=0, \tag{4}$$

at any point in space and time.

Based on the above BGK model as Eq. (1), the Euler equations can be obtained for a local equilibrium state with $f=g$. On the other hand, the Navier-Stokes equations, the stress and Fourier heat conduction terms can be derived with the Chapman-Enskog expansion [44] truncated to the 1st-order of τ,

$$f=g+Knf_1=g-\tau(\frac{\partial g}{\partial t}+u\frac{\partial g}{\partial x}+v\frac{\partial g}{\partial y}+w\frac{\partial g}{\partial z}). \tag{5}$$

For the Burnett and super-Burnett solutions, the above expansion can be naturally extended [45], such as $f=g+Knf_1+Kn^2f_2+Kn^3f_3+\cdots$. For the above Navier-Stokes solutions, the GKS based on the kinetic BGK model has been well developed [21]. In order to simulate the flow with any realistic Prandtl number, a modification of the heat flux in the energy transport is used in this scheme, which is also implemented in the present study.

Taking moments of Eq. (1) and integrating over the control volume $\Omega_{ijk}=\overline{x_i}\times\overline{y_j}\times\overline{z_k}$ with $\overline{x_i}=[x_i-\frac{\Delta x}{2},x_i+\frac{\Delta x}{2}]$, $\overline{y_j}=[y_j-\frac{\Delta y}{2},y_j+\frac{\Delta y}{2}]$, $\overline{z_k}=[z_k-\frac{\Delta z}{2},z_k+\frac{\Delta z}{2}]$, the three-dimensional finite volume scheme can be written as

$$\frac{dQ_{ijk}}{dt}=\mathbf{L}(Q_{ijk})=\frac{1}{|\Omega_{ijk}|}[\int_{\overline{y_j}\times\overline{z_k}}(F_{i-1/2,j,k}-F_{i+1/2,j,k})dydz$$

$$+\int_{\overline{x_i}\times\overline{z_k}}(G_{i,j-1/2,k}-G_{i,j+1/2,k})dxdz$$
$$+\int_{\overline{x_i}\times\overline{y_j}}(H_{i,j,k-1/2}-H_{i,j,k+1/2})dxdy], \quad (6)$$

where Q_{ijk} are the cell averaged conservative flow variables, i.e., mass, momentum and total energy. All of them are averaged over control volume Ω_{ijk} and the volume of the numerical cell is $|\Omega_{ijk}| = \Delta x\Delta y\Delta z$. Here, numerical fluxes in $x-$direction is presented as an example

$$\int_{\overline{y_j}\times\overline{z_k}} F_{i+1/2,j,k}dydz = F_{\mathbf{x}_{i+1/2,j,k},t}\Delta y\Delta z. \quad (7)$$

Based on the fifth-order WENO-JS spatial reconstruction on the primitive flow variables [46], the reconstructed point value and the spatial derivatives in one normal and two tangential directions can be obtained. In the smooth flow computation, the linear form of WENO-JS is adopted to reduce the dissipation. Gaussian points are widely used for high-order finite volume scheme, however, it is very expensive because additional reconstructions and flux calculations are required at each point of the interface [39]. To save computational resources for three-dimensional high-Reynolds number engineering turbulence problems, Gaussian points have not been used in the IHGKS. The numerical fluxes $F_{\mathbf{x}_{i+1/2,j,k},t}$ can be provided by the flow solvers, which can be evaluated by taking moments of the gas distribution function as

$$F_{\mathbf{x}_{i+1/2,j,k},t} = \int \psi_\alpha u f(\mathbf{x}_{i+1/2,j,k},t,\mathbf{u},\xi)d\Xi, \quad \alpha = 1,2,3,4,5. \quad (8)$$

Here $f(\mathbf{x}_{i+1/2,j,k},t,\mathbf{u},\xi)$ is based on the integral solution of BGK equation Eq. (1) at the cell interface

$$f(\mathbf{x}_{i+1/2,j,k},t,\mathbf{u},\xi) = \frac{1}{\tau}\int_0^t g(\mathbf{x}',t',\mathbf{u},\xi)e^{-(t-t')/\tau}dt' + e^{-t/\tau}f_0(-\mathbf{u}t,\xi), \quad (9)$$

where $\mathbf{x}_{i+1/2,j,k} = \mathbf{0}$ is the location of cell interface, $\mathbf{u} = (u,v,w)$ is the particle velocity, $\mathbf{x}_{i+1/2,j,k} = \mathbf{x}' + \mathbf{u}(t-t')$ is the trajectory of particles. f_0 is the initial gas distribution, and g is the corresponding intermediate equilibrium state as Eq. (2). g and f_0 can be constructed as

$$g = g_0(1+\overline{a}x+\overline{b}y+\overline{c}z+\overline{A}t),$$

and

$$f_0 = \begin{cases} g_l[1+(a_lx+b_ly+c_lz)-\tau(a_lu+b_lv+c_lw+A_l)], & x\le 0,\\ g_r[1+(a_rx+b_ry+c_rz)-\tau(a_ru+b_rv+c_rw+A_r)], & x>0, \end{cases}$$

where g_l and g_r are the initial gas distribution functions on both sides of a cell interface. g_0 is the initial intermediate equilibrium state located at cell interface, which can be determined through the compatibility condition

$$\int \psi_\alpha g_0 d\Xi = \int_{u>0}\psi_\alpha g_l d\Xi + \int_{u<0}\psi_\alpha g_r d\Xi, \quad \alpha = 1,2,3,4,5.$$

For the second-order flux, the time-dependent gas distribution function at cell interfaces is evaluated as

$$\begin{aligned} f(\mathbf{x}_{i+1/2,j,k},t,\mathbf{u},\xi) &= (1-e^{-t/\tau})g_0 + ((t+\tau)e^{-t\tau}-\tau)(\overline{a}u+\overline{b}v+\overline{c}w)g_0 \\ &+ (t-\tau+\tau e^{-t\tau})\overline{A}g_0 \\ &+ e^{-t/\tau}g_l[1-(\tau+t)(a_lu+b_lv+c_lw)-\tau A_l](1-H(u)) \\ &+ e^{-t/\tau}g_r[1-(\tau+t)(a_ru+b_rv+c_rw)-\tau A_r]H(u), \end{aligned} \quad (10)$$

where the coefficients in Eq. (10) can be determined by the spatial derivatives of macroscopic flow variables and the compatibility condition [22]. In smooth flow region, the discontinuities of flow variables at a cell interface disappear, and the gas distribution function at a cell interface $f(\mathbf{x}_{i+1/2,j,k},t,\mathbf{u},\xi)$ automatically reduces to

$$f(\mathbf{x}_{i+1/2,j,k},t,\mathbf{u},\xi) = g_0[1-\tau(\overline{a}u+\overline{b}v+\overline{c}w+\overline{A})+t\overline{A}]. \quad (11)$$

The full flux Eq. (10) is necessary for shock-capturing, which must be used for transonic to supersonic flows. While, Eq. (11) is applied in smooth flows, and the computational costs can be reduced.

Here, the second-order accuracy in time can be achieved by one step integration from the second-order gas-kinetic solver Eq. (10). Based on a high-order expansion of the equilibrium state around a cell interface, a one-stage third-order GKS has been developed successfully [24,47,48]. However, the one-stage gas-kinetic solver becomes very complicated, especially for three-dimensional computations.

2.2. Two-stage high-order temporal discretization

In recent study, a two-stage fourth-order time-accurate discretization has been developed for Lax-Wendroff flow solvers, particularly applied for hyperbolic equations with the generalized Riemann problem (GRP) solver [38] and the GKS [39]. Such method provides a reliable framework to develop the three-dimensional IHGKS with a second-order flux function Eq. (10) or Eq. (11). The key point for this two-stage fourth-order method is to use time derivative of flux function. In order to obtain the time derivative of flux function at t_n and $t_* = t_n + \Delta t/2$, the flux function should be approximated as a linear function of time within a time interval.

According to the numerical fluxes Eq. (8) at a cell interface, the following notation is introduced

$$\mathbb{F}_{i+1/2,j,k}(Q^n,\zeta) = \int_{t_n}^{t_n+\zeta}\mathbf{F}_{i+1/2,j,k}(Q^n,t)dt = \int_{t_n}^{t_n+\zeta}F_{\mathbf{x}_{i+1/2,j,k},t}dt. \quad (12)$$

In the time interval $[t_n, t_n+\Delta t/2]$, the flux is expanded as the following linear form

$$\mathbf{F}_{i+1/2,j,k}(Q^n,t) = \mathbf{F}_{i+1/2,j,k}(Q^n,t_n) + \partial_t\mathbf{F}_{i+1/2,j,k}(Q^n,t_n)(t-t_n). \quad (13)$$

Based on Eq. (12) and linear expansion of flux as Eq. (13), the coefficients $\mathbf{F}_{i+1/2,j,k}(Q^n,t_n)$ and $\partial_t\mathbf{F}_{i+1/2,j,k}(Q^n,t_n)$ can be determined as,

$$\begin{aligned} &\mathbf{F}_{i+1/2,j,k}(Q^n,t_n)\Delta t + \frac{1}{2}\partial_t\mathbf{F}_{i+1/2,j,k}(Q^n,t_n)\Delta t^2 \\ &\quad = \mathbb{F}_{i+1/2,j,k}(Q^n,\Delta t), \\ &\frac{1}{2}\mathbf{F}_{i+1/2,j,k}(Q^n,t_n)\Delta t + \frac{1}{8}\partial_t\mathbf{F}_{i+1/2,j,k}(Q^n,t_n)\Delta t^2 \\ &\quad = \mathbb{F}_{i+1/2,j,k}(Q^n,\Delta t/2). \end{aligned}$$

By solving the linear system, we have

$$\begin{aligned}\mathbf{F}_{i+1/2,j,k}(Q^n,t_n) &= (4\mathbb{F}_{i+1/2,j,k}(Q^n,\Delta t/2)\\ &\quad -\mathbb{F}_{i+1/2,j,k}(Q^n,\Delta t))/\Delta t,\\ \partial_t\mathbf{F}_{i+1/2,j,k}(Q^n,t_n) &= 4(\mathbb{F}_{i+1/2,j,k}(Q^n,\Delta t)\\ &\quad -2\mathbb{F}_{i+1/2,j,k}(Q^n,\Delta t/2))/\Delta t^2,\end{aligned} \tag{14}$$

and $\mathbf{F}_{i+1/2,j,k}(Q^*,t_*)$, $\partial_t\mathbf{F}_{i+1/2,j,k}(Q^*,t_*)$ for the intermediate state t_* can be constructed similarly.

With these notations, the two-stage high-order algorithm for three-dimensional flow is given by the following steps.

(i) With the initial reconstruction, update Q^*_{ijk} at $t_*=t_n+\Delta t/2$ by

$$\begin{aligned}Q^*_{ijk}-Q^n_{ijk} &= -\frac{1}{\Delta x}[\mathbb{F}_{i+1/2,j,k}(Q^n,\Delta t/2)-\mathbb{F}_{i-1/2,j,k}(Q^n,\Delta t/2)]\\ &\quad -\frac{1}{\Delta y}[\mathbb{G}_{i,j+1/2,k}(Q^n,\Delta t/2)-\mathbb{G}_{i,j-1/2,k}(Q^n,\Delta t/2)]\\ &\quad -\frac{1}{\Delta z}[\mathbb{H}_{i,j,k+1/2}(Q^n,\Delta t/2)-\mathbb{H}_{i,j,k-1/2}(Q^n,\Delta t/2)],\end{aligned} \tag{15}$$

and compute the fluxes and their derivatives by Eq. (14) for future using,

$$\mathbf{F}_{i+1/2,j,k}(Q^n,t_n),\ \mathbf{G}_{i,j+1/2,k}(Q^n,t_n),\ \mathbf{H}_{i,j,k+1/2}(Q^n,t_n),$$
$$\partial_t\mathbf{F}_{i+1/2,j,k}(Q^n,t_n),\ \partial_t\mathbf{G}_{i,j+1/2,k}(Q^n,t_n),\ \partial_t\mathbf{H}_{i,j,k+1/2}(Q^n,t_n).$$

(ii) Reconstruct intermediate value W^*_{ijk} and compute

$$\partial_t\mathbf{F}_{i+1/2,j,k}(Q^*,t_*),\ \partial_t\mathbf{G}_{i,j+1/2,k}(Q^*,t_*),\ \partial_t\mathbf{H}_{i,j,k+1/2}(Q^*,t_*),$$

where the derivatives are determined by Eq. (14) in the time interval $[t_*,t_*+\Delta t]$.

(iii) Update Q^{n+1}_{ijk} by

$$\begin{aligned}Q^{n+1}_{ijk}-Q^n_{ijk} &= -\frac{\Delta t}{\Delta x}[\overline{\mathbb{F}}^n_{i+1/2,j,k}-\overline{\mathbb{F}}^n_{i-1/2,j,k}]\\ &\quad -\frac{\Delta t}{\Delta y}[\overline{\mathbb{G}}^n_{i,j+1/2,k}-\overline{\mathbb{G}}^n_{i,j-1/2,k}]\\ &\quad -\frac{\Delta t}{\Delta z}[\overline{\mathbb{H}}^n_{i,j,k+1/2}-\overline{\mathbb{H}}^n_{i,j,k-1/2}],\end{aligned} \tag{16}$$

where $\overline{\mathbb{F}}^n_{i+1/2,j,k}$, $\overline{\mathbb{G}}^n_{i,j+1/2,k}$ and $\overline{\mathbb{H}}^n_{i,j,k+1/2}$ are the numerical fluxes and expressed as

$$\begin{aligned}\overline{\mathbb{F}}^n_{i+1/2,j,k} &= \mathbf{F}_{i+1/2,j,k}(Q^n,t_n)+\frac{\Delta t}{6}[\partial_t\mathbf{F}_{i+1/2,j,k}(Q^n,t_n)\\ &\quad +2\partial_t\mathbf{F}_{i+1/2,j,k}(Q^*,t_*)],\\ \overline{\mathbb{G}}^n_{i,j+1/2,k} &= \mathbf{G}_{i,j+1/2,k}(Q^n,t_n)+\frac{\Delta t}{6}[\partial_t\mathbf{G}_{i,j+1/2,k}(Q^n,t_n)\\ &\quad +2\partial_t\mathbf{G}_{i,j+1/2,k}(Q^*,t_*)],\\ \overline{\mathbb{H}}^n_{i,j,k+1/2} &= \mathbf{H}_{i,j,k+1/2}(Q^n,t_n)+\frac{\Delta t}{6}[\partial_t\mathbf{H}_{i,j,k+1/2}(Q^n,t_n)\\ &\quad +2\partial_t\mathbf{H}_{i,j,k+1/2}(Q^*,t_*)].\end{aligned}$$

In summary, with the initial reconstruction, the intermediate state Q^*_{ijk} is updated by

$$Q^*_{ijk}=Q^n_{ijk}+\frac{\Delta t}{2}\mathbf{L}^*(Q^n), \tag{17}$$

where $\frac{\Delta t}{2}\mathbf{L}^*(Q^n)$ represents the right-hand side of Eq. (15). Then, with the prepared fluxes and their derivatives, Q^{n+1}_{ijk} can be updated by

$$Q^{n+1}_{ijk}=Q^n_{ijk}+\Delta t\mathbf{L}^{n+1}(Q^n), \tag{18}$$

where $\Delta t\mathbf{L}^{n+1}(Q^n)$ is the right-hand side terms in Eq. (16). $\mathbf{L}$ is the spatial discretization operator as Eq. (6).

2.3. Implicit LU-SGS method

In previous work, LU-SGS method has been applied in GKS for hypersonic flows [49] and near-continuum flows [50] in two-dimensional cases. For three-dimensional flow, in order to use large CFL number to increase the computational efficiency, instead of updating conservative variables explicitly, implicit LU-SGS method is used to update conservative variables Q^*_{ijk} and Q^{n+1}_{ijk}. As an example, in the following we present the brief updating procedure of intermediate variables Q^*.

Firstly, introduce the Jacobian matrices $\mathcal{A}=\frac{\partial F}{\partial Q}_i$, $\mathcal{B}=\frac{\partial F}{\partial Q}_j$, and $\mathcal{C}=\frac{\partial F}{\partial Q}_k$, with the Euler flux F for laminar flow [41] and the extended flux coupled with turbulence model [42]. Based on the LU-SGS technique, Eq. (17) can be written as

$$\begin{aligned}\mathbf{R}^*(Q^n) &= \frac{\Delta t}{2}\mathbf{L}^*(Q^n),\\ (L+D)D^{-1}(D+U)\Delta Q &= \mathbf{R}^*(Q^n),\end{aligned} \tag{19}$$

where $\Delta Q=Q^*-Q^n$, with the matrices $L=-(\mathcal{A}^+_{i-1}+\mathcal{B}^+_{j-1}+\mathcal{C}^+_{k-1})$, $D=\frac{\mathcal{I}}{\Delta t}+\mathcal{A}^+_i-\mathcal{A}^-_i+\mathcal{B}^+_j-\mathcal{B}^-_j+\mathcal{C}^+_k-\mathcal{C}^-_k$, and $U=\mathcal{A}^-_{i+1}+\mathcal{B}^-_{j+1}+\mathcal{C}^-_{k+1}$. Unknown matrices are introduced by $\mathcal{A}^\pm=\frac{1}{2}(\mathcal{A}\pm r_\mathcal{A}\mathcal{I}), r_\mathcal{A}=\beta\sigma_\mathcal{A}$, $\mathcal{B}^\pm=\frac{1}{2}(\mathcal{B}\pm r_\mathcal{B}\mathcal{I}), r_\mathcal{B}=\beta\sigma_\mathcal{B}$, and $\mathcal{C}^\pm=\frac{1}{2}(\mathcal{C}\pm r_\mathcal{C}\mathcal{I}), r_\mathcal{C}=\beta\sigma_\mathcal{C}$. Where $\mathcal{I}$ is the unit matrix, $(\sigma_\mathcal{A},\sigma_\mathcal{B},\sigma_\mathcal{C})$ are the spectral radii of the Jacobian matrices, with the coefficient $\beta\geq 1$ to ensure dominant diagonal.

Then, use two-step sweeping way to get the solution ΔQ

$$\begin{aligned}(L+D)\Delta Q^\circ &= \mathbf{R}^*(Q^n),\\ (D+U)\Delta Q &= D\Delta Q^\circ.\end{aligned} \tag{20}$$

Subsequently, the intermediate macroscopic flow variables Q^* are updated by

$$Q^*=Q^n+\Delta Q. \tag{21}$$

Based on Eq. (18), the residual at t_{n+1} step is defined as $\mathbf{R}^{n+1}(Q^n)=\Delta t\mathbf{L}^{n+1}(Q^n)$. Then, similar procedures as Eq. (19)–Eq. (21) can be used to update the t_{n+1} step macroscopic flow variables Q^{n+1}. In this way, within the S2O4 GKS framework, LU-SGS method is implemented to overcome the time step barrier in the explicit scheme.

3. IHGKS coupled with turbulence model

We follow the concept of turbulent eddy viscosity [51], which models the effect of unresolved turbulent scales by enlarged turbulent eddy viscosity in turbulence region. Similarly, the enlarged turbulent relaxation time τ_t is proposed to describe the turbulent flows under the kinetic framework. Based on this turbulent relaxation time τ_t [31], extended BGK model for turbulent flows can be written as,

$$\frac{\partial f}{\partial t}+u\frac{\partial f}{\partial x}+v\frac{\partial f}{\partial y}+w\frac{\partial f}{\partial z}=\frac{g-f}{\tau+\tau_t}. \tag{22}$$

Using the Chapman-Enskog expansion [32], Eq. (22) can recover traditional RANS linear eddy viscosity model through the relation between turbulent eddy viscosity μ_t and turbulent relaxation time τ_t, with

$$\tau+\tau_t=\frac{\mu+\mu_t}{p}, \tag{23}$$

where p is the pressure. The key point is to get turbulent eddy viscosity μ_t, then turbulent relaxation time τ_t will be determined

by Eq. (23). In original study [32], this enlarged relaxation time τ_t is called "mixing time", which is comparable with the classical concept of "mixing length". In this paper, based on extended BGK model and "mixing time" concept, time-relaxation turbulence simulation will be studied.

In present work, Vreman-type model for LES and $k-\omega$ SST model for RANS simulation will be used to evaluate τ_t and use the relaxation time $\tau+\tau_t$ in Eq. (22). All conserved macroscopic variables are calculated from GKS, and the turbulent viscosity is obtained from the LES/RANS eddy viscosity model. The evolution of turbulent variables depends on the conserved macroscopic variables. This coupling process is applied at each step for turbulence simulations.

3.1. LES: Vreman-type model

To keep the simple eddy viscosity closure form and overcome the drawbacks of the original Smagorinsky model [13], Vreman-type model [15] is proposed by A.W. Vreman in a simple algebra form, which is comparable to dynamic Smagorinsky model [14]. For Vreman-type model, turbulent eddy viscosity μ_t is given by

$$\mu_t = \rho c \sqrt{\frac{B_\beta}{a_{ij}a_{ij}}}, \tag{24}$$

where ρ is the density, and constant c is related to Smagorinsky constant $c = 2.5C_s^2$, with $C_s = 0.1$. Left unknowns in Eq. (24) can be determined through the combination of velocity gradient in resolved flow fields, as

$$\begin{cases} \alpha_{ij} &= \frac{\partial U_j}{\partial x_i}, \\ \beta_{ij} &= \Delta^2 \alpha_{mi}\alpha_{mj}, \\ B_\beta &= \beta_{11}\beta_{22} - \beta_{12}^2 + \beta_{11}\beta_{33} - \beta_{13}^2 + \beta_{22}\beta_{33} - \beta_{23}^2. \end{cases} \tag{25}$$

In Eq. (25), the $\frac{\partial U_j}{\partial x_i}$ represents the first-order derivative of cell averaged velocity, and Δ is the width of the numerical cell. For averaging process, numerical cell itself acts as the filter and no explicit filter is adopted in current scheme.

3.2. RANS: $k-\omega$ SST model

$k-\omega$ SST model [10] combines the positive features of $k-\omega$ model [8] and $k-\epsilon$ model [7] together. For this model, evolution equation of turbulence kinetic energy k and specific dissipation rate ω are modeled as

$$\begin{aligned} &\frac{\partial(\rho k)}{\partial t} + \frac{\partial}{\partial x_j}[\rho U_j k - (\mu + \sigma_k \mu_t)\frac{\partial k}{\partial x_j}] = P - \beta^* \rho \omega k, \\ &\frac{\partial(\rho \omega)}{\partial t} + \frac{\partial}{\partial x_j}[\rho u_j \omega - (\mu + \sigma_\omega \mu_t)\frac{\partial \omega}{\partial x_j}] \\ &= \frac{\gamma}{\nu_t} P - \beta \rho \omega^2 + 2(1-F_1)\frac{\rho \sigma_{\omega 2}}{\omega}\frac{\partial k}{\partial x_j}\frac{\partial \omega}{\partial x_j}, \end{aligned} \tag{26}$$

where P is the production of turbulence kinetic energy. In current study, P is written in SST-V2003 form [11], as

$$\begin{aligned} P^* &= \mu_t \Omega^2 - \frac{2}{3}\rho k \delta_{ij}\frac{\partial U_i}{\partial x_j}, \\ P &= min(P^*, 10\beta^* \rho \omega k), \end{aligned}$$

where $\Omega = \sqrt{2\Omega_{ij}\Omega_{ij}}$ is the vorticity magnitude. The turbulent eddy viscosity is computed from

$$\mu_t = \frac{\rho a_1 k}{max\{a_1 \omega, SF_2\}}, \tag{27}$$

where $\nu_t = \mu_t/\rho$ is the turbulent kinematic viscosity, $S = \sqrt{2S_{ij}S_{ij}}$ is the shear strain rate magnitude. Ω_{ij} and S_{ij} are denoted by

$$\Omega_{ij} = \frac{1}{2}(\frac{\partial U_i}{\partial x_j} - \frac{\partial U_j}{\partial x_i}),\ S_{ij} = \frac{1}{2}(\frac{\partial U_i}{\partial x_j} + \frac{\partial U_j}{\partial x_i}).$$

Each of the constants is a blend of an inner constant and outer constant via

$$\phi = F_1\phi_1 + (1-F_1)\phi_2, \quad (\phi = \sigma_k, \sigma_\omega, \beta, \gamma)$$

where ϕ_1 represents the inner constants of $k-\omega$ model and ϕ_2 represents the outer constants of the $k-\epsilon$ model. For inner layer,

$$\sigma_{k1} = 0.85,\ \sigma_{\omega 1} = 0.5,\ \beta_1 = 0.075,\ \gamma_1 = \frac{5}{9},$$

and for outer layer,

$$\sigma_{k2} = 1.0,\ \sigma_{\omega 2} = 0.856,\ \beta_2 = 0.0828,\ \gamma_2 = 0.44.$$

F_1 and F_2 are hybrid functions are given by

$$F_1 = \tanh\{min[max(\frac{\sqrt{k}}{\beta^* \omega d}, \frac{500\mu}{\rho \omega d^2}), \frac{4\rho\sigma_{\omega 2}k}{CD_{k\omega}d^2}]\}^4,$$

$$F_2 = \tanh[max(\frac{2\sqrt{k}}{0.09\omega d}, \frac{500\mu}{\rho\omega d^2})]^2,$$

$$CD_{k\omega} = max(\frac{2\rho\sigma_{\omega 2}}{\omega}\frac{\partial k}{\partial x_j}\frac{\partial \omega}{\partial x_j}, 10^{-10}),$$

where d is the colsest distance from the field point to the nearest wall, and left constants are $a_1 = 0.31$ and $\beta^* = 0.09$.

In this paper, turbulent variables k and ω are updated separately from the conservative variables in the GKS. Because turbulent modeling error is dominant in RANS simulation, there is no special high-order reconstruction for Eq. (26). In current study, incorporated with the second-order GKS for conservative flow variables, the turbulent equations are solved with first-order upwind reconstruction and Roe scheme [52] for advection terms. When coupled with the high-order GKS, the turbulent models are solved by WENO-JS reconstruction and Roe scheme. Considering the source terms are quiet stiff for $k-\omega$ SST model, second-order central difference is used for source terms in Eq. (26).

4. Numerical tests

In this section, numerical tests from the fundamental homogeneous isotropic turbulence to the high-Reynolds number engineering turbulent flows will be presented to validate current extended BGK model and implicit high-order numerical scheme. The smooth flows are used to validate the high-accuracy solution in space and time obtained by the high-order GKS, and transonic practical turbulent flows are designed to address the high-efficiency and robustness of current IHGKS. For following simulation, the collision time takes

$$\tau + \tau_t = \frac{\mu + \mu_t}{p} + C\frac{|p_l - p_r|}{|p_l + p_r|}\Delta t,$$

where μ is the viscous coefficient obtained from Sutherland's Law, μ_t comes from the turbulence model, and p is the pressure at the interface. C is set to be 1.5 in the computation, p_l and p_r denote the pressures on the left and right sides at the cell interface. Δt is the time step which is determined according to the CFL condition.

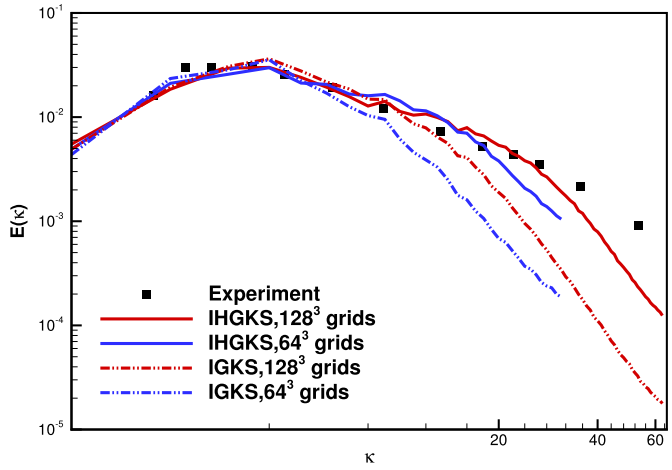

Fig. 1. Spectral of TKE at dimensionless time $t^* = 0.87$ with the experiment data, the IHGKS and the second-order IGKS. (For interpretation of the colors in the figure(s), the reader is referred to the web version of this article.)

4.1. LES case: incompressible decaying homogeneous isotropic turbulence

Incompressible decaying homogeneous isotropic turbulence (IDHIT) is the most fundamental turbulent flow, a classical system for turbulence theory [53]. Additionally, IDHIT is widely used to validate turbulence model and is regarded as a benchmark to verify the performance of high-order scheme. In current study, the reference experiment is conducted by Comte-Bellot et al. [54], with Taylor Reynolds number $Re_\lambda = 71.6$ and turbulent Mach number $Ma_t = 0.2$. In numerical simulation, computation domain is a $(2\pi)^3$ box with 64^3 and 128^3 uniform grids, and periodic boundary condition in 6 faces are applied. The initial turbulent fluctuating velocity fields is computed from experimental energy spectral, with constant pressure, density and temperature.

The turbulent fluctuating velocity u', the Taylor microscale λ, the Taylor Reynolds number Re_λ, the turbulent Mach number Ma_t, and the spectral of turbulence kinetic energy (TKE) are defined as

$$u' = < (u_1^2 + u_2^2 + u_3^2)/3 >^{1/2},$$

$$\lambda^2 = \frac{u'^2}{< (\partial u_1/\partial x_1)^2 >},$$

$$Re_\lambda = \frac{u'\lambda}{\nu},$$

$$Ma_t = \frac{< u_1^2 + u_2^2 + u_3^2 >^{1/2}}{a},$$

$$E(\kappa) = \frac{1}{2}\int_{\kappa_{min}}^{\kappa_{max}} \Phi_{ii}(\boldsymbol{\kappa})\delta(|\boldsymbol{\kappa}| - \kappa)d\boldsymbol{\kappa},$$

where $< \cdots >$ represents the space average in computation domain. u_1, u_2, and u_3 are three components for turbulent fluctuating velocity. Here, a represents the local sound speed, and ν represents the kinematic viscosity as μ/ρ. Velocity spectral Φ_{ii} is the Fourier transform of two-point correlation, with wave number $\kappa_{min} = 0$ and $\kappa_{max} = N/2$, where N is the number of grid points in each direction of box.

For this unsteady flow, dual-step method has not been implemented in current implicit scheme, so CFL number is adopted similar as the explicit scheme $CFL = 0.15$. Current IHGKS and the second-order implicit GKS (IGKS) with Vreman-type LES model on 64^3 and 128^3 grids are performed, using the smooth flux as Eq. (11). Fig. 1 shows the spectral of TKE at dimensionless time $t^* = 0.87$, from the IHGKS and the second-order IGKS. All schemes behave well in low wavenumber region, and large-scale turbulent structure are resolved. With the same grid, from the moderate wavenumber region to the high wavenumber region, TKE spectral from the high-order scheme is much closer to the experimental result, which outweighs results from the second-order scheme. In particular, it is clear that result from the high-order scheme on 64^3 grids even performs better than that from the second-order scheme on 128^3 grids. TKE spectral indicates that current IHGKS obtains more accurate turbulent flow fields on coarse 64^3 grids, and the second-order GKS is more dissipative. Balancing well between the accuracy and computational costs, the IHGKS without Gaussian points is an appropriate trade-off for following engineering turbulence simulation.

Table 1
Grid information of grid G1 and grid G2.

Solver	Grid	Nx × Ny	Total grid	Y^+_{plate}
IHGKS/HGKS	G1	273 × 193	5.26×10^4	0.2
CFL3D	G2	543 × 385	2.10×10^5	0.08

Table 2
Maximum CFL number for the IHGKS and the explicit HGKS.

Solver	Grid	CFL number	CPU time
IHGKS	G1	2.50	0.56s/each step
HGKS	G1	0.15	0.51s/each step

4.2. RANS 2D case: incompressible turbulence with zero pressure gradient over a flat plate

Two-dimensional zero pressure gradient turbulence over flat plate is used to test the high efficiency of current IHGKS compared with the explicit HGKS. This is one of turbulence model verification test cases provided by the NASA turbulence modeling resource (TMR) [55]. In current case, free stream condition is Mach number $Ma = 0.2$, and Reynolds number $Re = 5.0 \times 10^6$ with reference length 1.0. The computational domain and boundary conditions are adopted as the NASA's website. As presented in Table 1, CFL3D is implemented on fine grid G2 which provides the reference results, while the IHGKS and the explicit HGKS are performed on moderate grid G1. The total grid of G2 is almost 4 times more than that of G1, and a smaller Y^+_{plate} is used in G2. Here, Y^+_{plate} is the non-dimensional wall distance for the first level grid upon the plate wall.

Moderate grid G1 is split into 5 blocks for parallel computing on Intel Xeon E5-2962 v2 cores. As Table 2 shows, the maximum CFL number which can be used for the IHGKS is $CFL = 2.5$, however, the explicit HGKS only can reach the maximum CFL number $CFL = 0.15$. With the smooth flux as Eq. (11), the CPU time/each step of the IHGKS is 0.56s/each step, which is slightly longer than that of the explicit HGKS. In Fig. 2, total residual and residual of $k-\omega$ convergence curves of these two schemes are plotted. Fig. 2 (a) shows the total residual converging rate of the IHGKS is much faster than that of the explicit HGKS. While, turbulent variables $k-\omega$ are quiet stiff as Fig. 2 (b) presents. Taking the CPU time/each step and the total residual converging rate into consideration, the IHGKS can speed up more than 10 times than the explicit HGKS. The significant acceleration on computational efficiency obtained by implicit LU-SGS method is pretty important when implementing engineering turbulence using high-order GKS. In the following cases, considering the affordable computational costs, only the IHGKS and the second-order IGKS will be implemented for high-Reynolds number turbulent flows.

To validate current implementation of $k-\omega$ SST model, it is legitimate to compare the TKE k and specific dissipation rate ω with

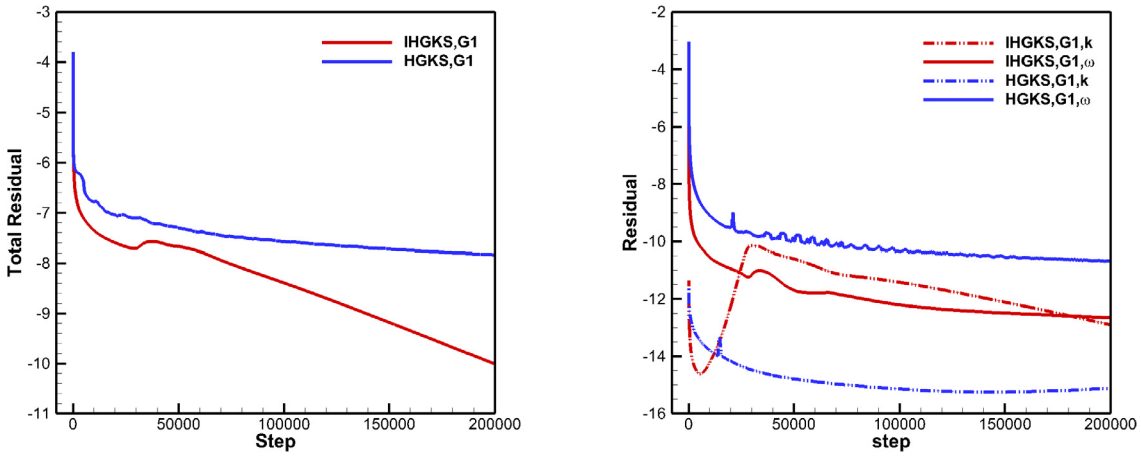

Fig. 2. Total residual and residual of $k-\omega$ convergence curves for the IHGKS and the explicit HGKS.

reference solutions firstly. Fig. 3 shows that the non-dimensional TKE k and specific dissipation rate ω of the IHGKS on moderate grid G1 agree well with the CFL3D on fine grid G2. Friction coefficient is provided for quantitative comparisons in Fig. 4. Overall, skin friction coefficients along the flat plate with the IHGKS and the second-order IGKS are comparable in Fig. 4 (a). As shown in Fig. 4 (b), compared with the reference solution on fine grid G2, current IHGKS predicts the transition region well, roughly from leading edge $X = 0$ to $X = 0.02$. For the second-order IGKS, this transition region has not been captured, which behaves similarly with previous second-order GKS simulation results [36]. Current case not only validates the high-efficiency of the IHGKS, but also indicates that the high-accuracy flow fields obtained by the IHGKS is required on moderate grid, such as transition prediction.

4.3. RANS 2D case: incompressible turbulence around NACA0012 airfoil

Engineering simulation of the incompressible NACA0012 airfoil with angle of attack $\alpha = 15^o$ is implemented, and the free stream condition is Mach number $Ma = 0.15$, Reynolds number $Re = 3.0 \times 10^6$ with the reference chord length $c = 1.0$. For lift coefficient and drag coefficient study, the reference area is set as $area = 1$. This is another turbulence model verification test case provided by the NASA TMR [55], which involves wall curvature, and thus pressure gradients are no longer equal to zero as above incompressible flat plate turbulence. The computational domain and boundary conditions are used as the NASA's website. As shown in Table 3, current study is based on the coarse grid G3 with IHGKS/IGKS, and the referee data are from the fine grid G4 with CFL3D. The total grid of G4 is almost 16 times more than that of G3, and an approximate 2 times smaller Y^+_{wall} is used in fine grid G4. Here, Y^+_{wall} is the non-dimensional wall distance for the first level grid upon the NACA0012 airfoil. Coarse grid G3 arrangement around NACA0012 is presented in Fig. 5.

CFL number is adopted as $CFL = 8$ and the total residual reduces down to the 6 orders of magnitude. In Fig. 6, Mach number contour and contour of normalized viscosity μ_t/μ are presented with the IHGKS on corase grid G3. As Fig. 6 shows, the incompressible flow field is quite smooth, which is consistent with using the smooth flux as Eq. (11). Pressure coefficient distributions around airfoil and skin friction coefficient distributions on upper airfoil are presented in Fig. 7. Among several sets of experimental pressure data provided by NASA's website, data from Gregory et al. [56] is chosen for validation in current study. It is believed that the Gregory data are likely more two-dimensional and hence more appropriate for CFD validation of surface pressures. Fig. 7 (a) shows that pressure coefficients based on current IHGKS are much closer with the experimental data, which is better than the results from the second-order IGKS. As presented in Fig. 7 (b), the skin friction coefficients with the IHGKS agree quiet well with the reference data than those from the second-order IGKS. The drag coefficient C_D is very sensitive to the pressure and skin friction distribution around the airfoil. As presented in Table 4, the lift coefficient, the drag coefficient and lift-drag ratio L/D from the IHGKS are very close to the reference data with CFL3D on fine grid G4. Especially, the discrepancy on C_D is within 3 drag counts (0.0001), reaching the high-level requirement for engineering turbulence simulation. For the second-order IGKS on coarse gird G3, the lift coefficient is acceptable, while it over predicts the drag coefficient C_D by 17.7%, almost 40 drag counts. This significant improvement on drag coefficient with coarse grid, confirms the high-accuracy turbulent flow fields are obtained by current IHGKS.

4.4. RANS 2D case: transonic turbulence around RAE2822 airfoil

Transonic turbulence around RAE2822 airfoil with angle of attack $\alpha = 2.79^o$ is implemented, to validate the robustness of shock-capturing in transonic high-Reynolds number turbulence by current IHGKS. The free stream condition is Mach number $Ma = 0.729$, Reynolds number $Re = 6.5 \times 10^6$ with the reference chord length $c = 1.0$. This is one turbulence model verification benchmark provided by the NPARC Alliance CFD Verification and Validation Web Site (NPARC) [57]. The computational domain and boundary conditions are used as the NPARC website. As shown in Table 5, the IHGKS is implemented on the moderate grid G5 from the NPARC website with $Y^+_{wall} = 2.5$. Since no reference solution provided by the second-order CFL3D on fine grid, for grid-independent analysis, fine grid G6 and grid G7 with $Y^+_{wall} = 0.625$ are used for the second-order IGKS. The global and local grid arrangement of moderate grid G5 around RAE2822 are shown in Fig. 8.

CFL number is adopted as $CFL = 2$ and the total residual reduces down to the 4 orders of magnitude. In Fig. 9, Mach number contour and contour of normalized viscosity μ_t/μ are presented based on the IHGKS with moderate grid G5. For this kind of transonic flows, the full flux as Eq. (10) is necessary for shock-capturing. Fig. 9 (a) shows the shock and its interaction with the turbulent boundary layer, which verify the robustness of the scheme on the capturing of shock. In Fig. 9 (b), the maximum eddy viscosity region is located near the trailing edge, which is different with the turbulence around NACA0012 airfoil with high angle of attack in Fig. 6 (b). To compare numerical solution from IHGKS/IGKS quantitatively, pressure coefficient distributions

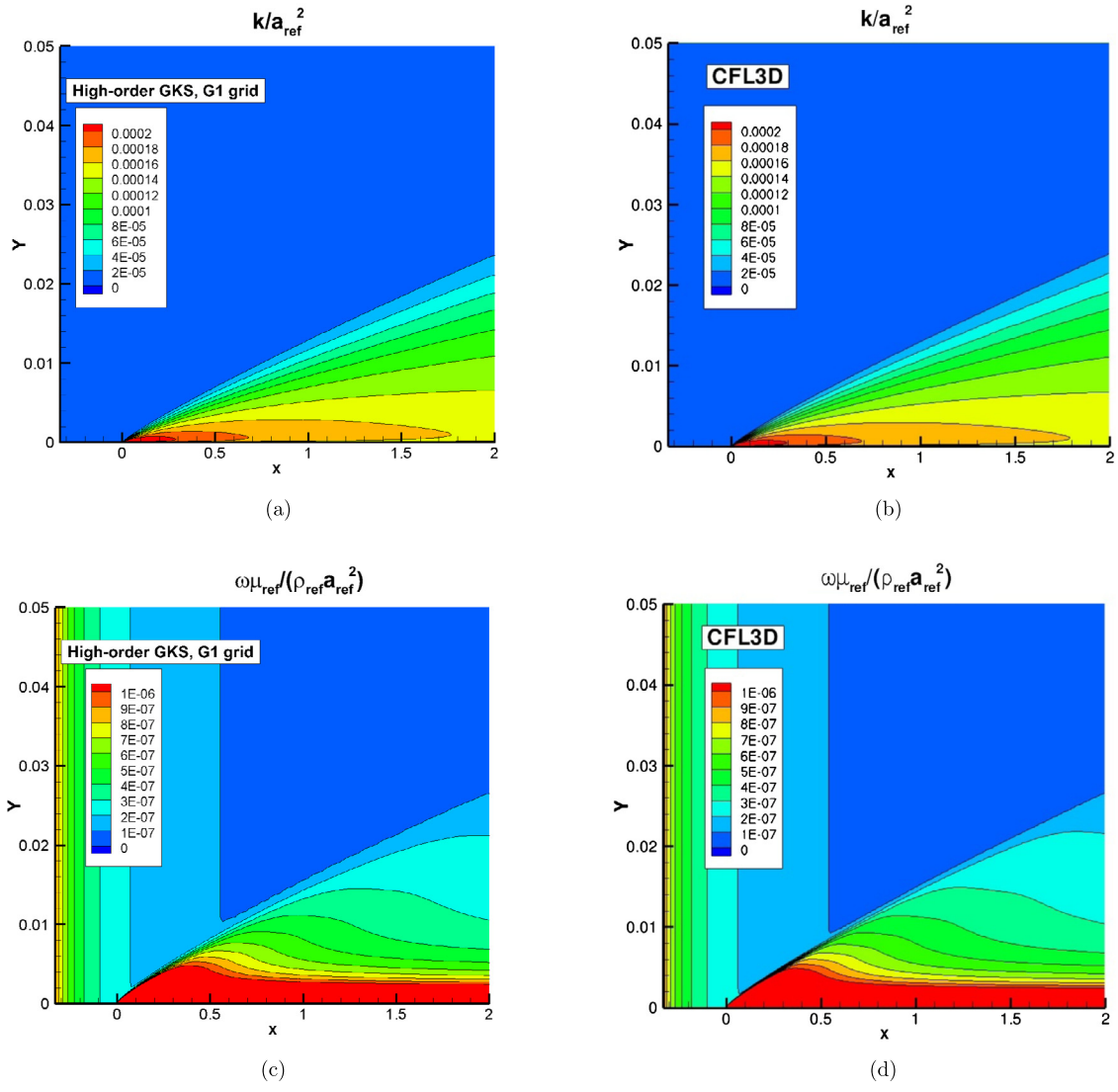

Fig. 3. Non-dimensional contours of TKE k and specific dissipation rate ω, (a) (c) from the IHGKS on moderate grid G1, and (b) (d) from the CFL3D on fine grid G2.

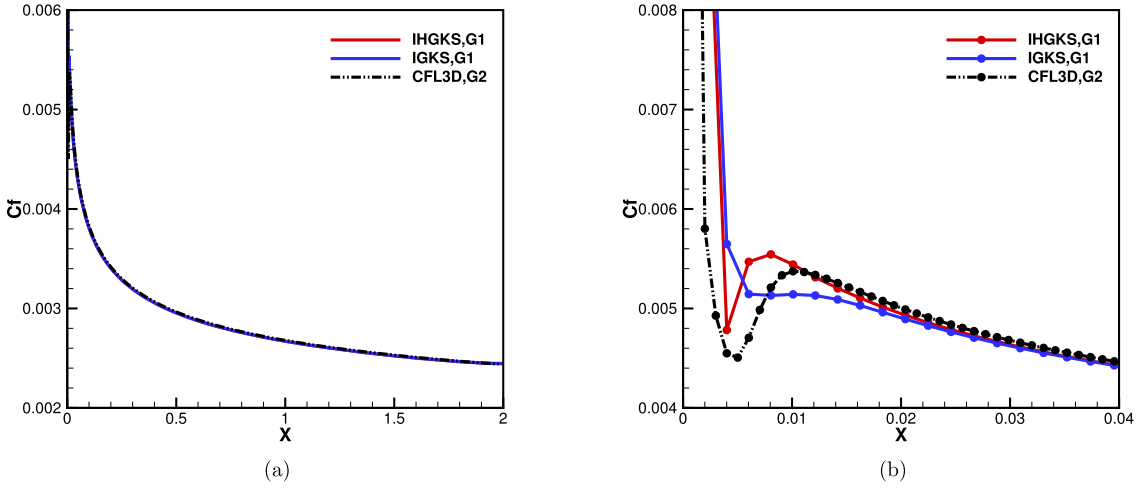

Fig. 4. Skin friction coefficient C_f along the flat plate (a) and within the local transitional region (b) from current IHGKS, the second-order IGKS, and the second-order CFL3D.

around airfoil and skin friction coefficient distributions on upper airfoil are presented in Fig. 10. As presented in Fig. 10, both the pressure coefficients and skin friction coefficients with the IHGKS and the second-order IGKS on moderate grid G5 match the experimental data from Cook et al. [58] well. This indicates turbulence model error dominates in this transonic flows instead of numeri-

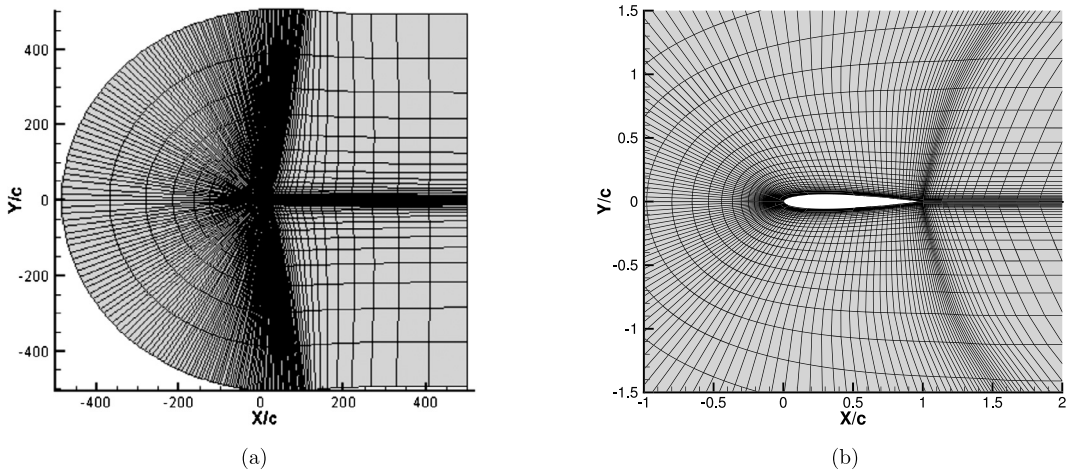

Fig. 5. Global arrangement (a) and local arrangement (b) of coarse grid G3 around NACA0012 airfoil. c is the chord length.

Table 3
Grid information of grid G3 and grid G4.

Solver	Grid	Nx × Ny	Total grid
IHGKS/IGKS	G3	225 × 65	1.46×10^4
CFL3D	G4	897 × 257	2.30×10^5

cal discretization error. To our expectation, on moderate grid G5, Fig. 10 (b) shows that skin friction coefficient with the IHGKS is slightly closer with the experiment data, compared with those using the second-order IGKS. Compared with the experimental data, Fig. 10 (a) shows the locations of the shock on fine grid G6 and G7 are slightly upstream than that on the moderate grid G5. For second-order GKS coupled with $k-\omega$ SST model on unstructured grid, the moderate grid with $Y^+_{wall} = 2.5$ provides a more reliable location of shock than that on a fine grid which has been reported in previous study [36]. While, the skin friction coefficient distributions on fine grid G6 and grid G7 with the second-order IGKS show the tendency to get close to the distribution by IHGKS on moderate grid G5. In view of the robustness of shock-capturing and better friction coefficient provided by the IHGKS, the high-order scheme is still preferred to predict accurate shock-boundary interaction in turbulent flows.

4.5. RANS 3D case: transonic ARA M100 wing-body turbulence

Three-dimensional transonic turbulence around complex configuration of ARA M100 wing-body is simulated. This case is adopted to keep studying the robustness of shock-capturing and validate the ability to simulate the three-dimensional real engineering turbulence by current IHGKS. Typical cruising condition of ARA M100 is the one corresponding to an angle of attack $\alpha = 2.873°$, Mach number $Ma = 0.8027$, and a local chord based Reynolds number of $Re_{lc} = 1.31 \times 10^7$ (local chord $lc = 0.245$). In this paper, the computational domain, the boundary conditions, and the C-O type grid of $321 \times 57 \times 49$ provided by CFL3D Version 6 website [59] are used, with an off wall Y^+ distribution as follows: $Y^+_{wing} = 0.8$, $0.1 \le Y^+_{fusel} \le 30$. Configuration of ARA M100 wing-body and surface grid are shown in Fig. 11, whose black part is the wing and the green part represents fuselage.

The maximum CFL number of the IHGKS is $CFL = 1.8$, while the CFL number of the explicit HGKS is limited by $CFL = 0.25$. For this complex three-dimensional transonic turbulent flow, the total residual reduces down to 4 orders of magnitude, with the full flux as Eq. (10). Fig. 12 shows streamlines on the upper wing surface and lower wing surface with pressure coefficient contours. As shown in Fig. 12 (a), the negative pressure coefficient regime is

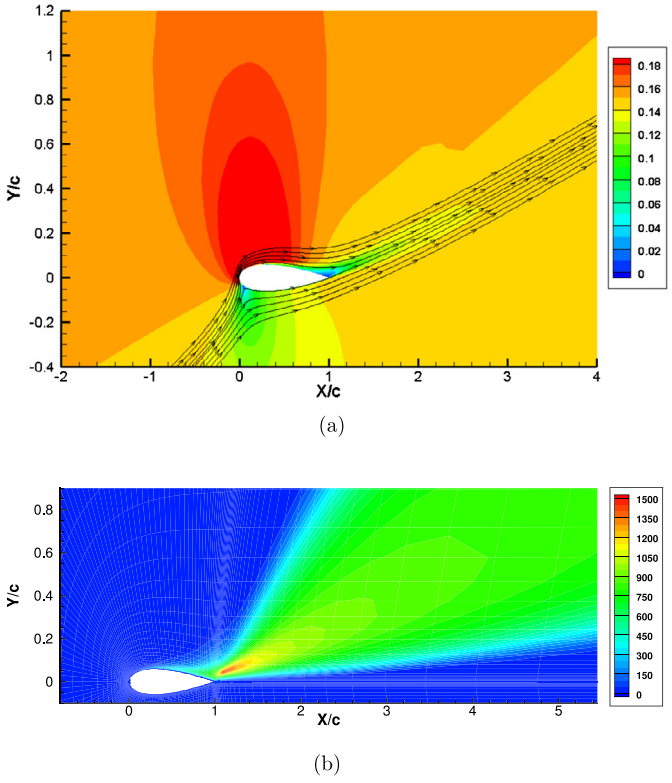

Fig. 6. Contours of Mach number (a) and normalized viscosity μ_t/μ (b) with the IHGKS on coarse grid G3 around NACA0012 airfoil.

followed by a reverse flow regime, involving adverse pressure gradients. The reverse flow regime is enclosed by separated streamline and reattached line on the wing's suction side, and no reverse flow regime appears in the lower wing surface as Fig. 12 (b). Mach number contours of one slice $Z/b = 0.019$ near the root chord plane and the slice $Z/b = 0.935$ near the wing's tip are presented in Fig. 13. These wing slices show the shock and its interaction with the turbulent boundary layer, which confirms the robustness of current scheme on the capturing of shock. The shock-boundary interaction is similar as above transonic RAE2822 turbulence in Fig. 9 (a). Comparisons of pressure coefficient Cp profiles at two selected wing sections among the experimental data from the CFL3D website, current IHGKS, the second-order IGKS, and results from CFL3D based on S-A model [9], are plotted in Fig. 14 at two selected wing sections cross the reverse flow regime. As the pres-

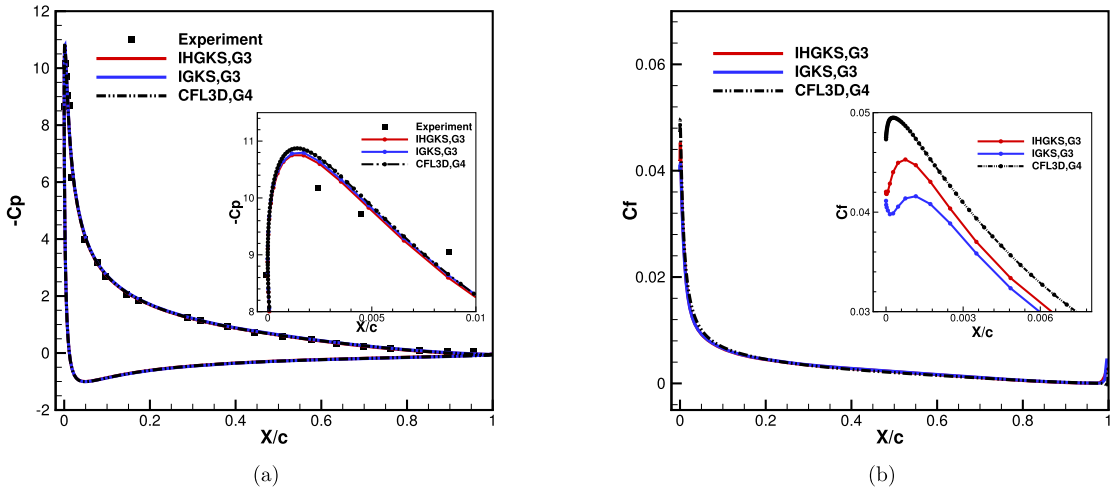

Fig. 7. Comparisons on pressure coefficient distributions Cp around airfoil (a) and skin friction coefficient C_f distributions on upper airfoil (b) from the experiment data, current IHGKS, the second-order IGKS, and the second-order CFL3D.

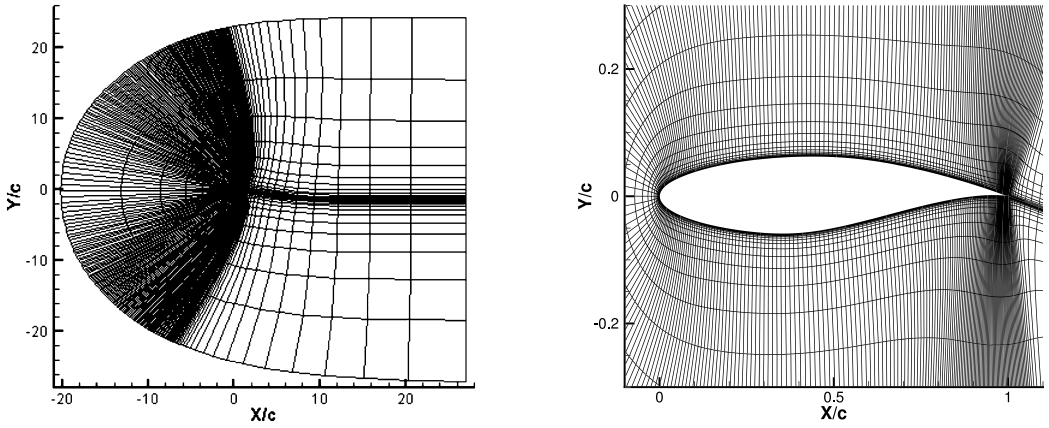

Fig. 8. Global gird arrangement (a) and local grid arrangement (b) of moderate grid G5 around RAE2822 airfoil.

Table 4
C_L and C_D for NACA0012.

Solver	IHGKS	IGKS	CFL3D
C_L	1.4930	1.5170	1.5060
C_D	0.02198	0.02618	0.02224
L/D	67.93	57.94	67.23

Table 5
Grid information of grid G5, grid G6 and grid G7.

Solver	Grid	Nx × Ny	Total grid	Y^+_{wall}
IHGKS/IGKS	G5	369 × 65	2.40×10^4	2.5
IGKS	G6	369 × 260	9.60×10^4	0.625
IGKS	G7	738 × 260	1.92×10^5	0.625

sure coefficient Cp from all schemes agree well with the experiment data, it confirms that both $k-\omega$ SST model and S-A model have the ability to predict pressure-induced separation. For different turbulence models, numerical results show that S-A model is a little better than $k-\omega$ SST model on lower wing surface, while $k-\omega$ SST model outweighs S-A model on the upper wing surface. In Fig. 14, compared with the obvious difference between different turbulence model, current IHGKS almost takes no advantage than the second-order IGKS. It is not surprising as the turbulence model error dominates in this transonic three-dimensional complex RANS simulation rather than the numerical discretization error. This indicates that developing appropriate turbulence model is still the most important task for three-dimensional complex RANS simulation. For transition flows [60,61], the turbulent model may play an even more important role.

5. Conclusion

In present work, targeting on accurate and efficient simulation of three-dimensional turbulent flows, an implicit high-order GKS with LU-SGS method is developed under the two-stage fourth-order framework. Vreman-type LES model for large eddy simulation and $k-\omega$ SST model for RANS simulation are coupled with current IHGKS. The cases of incompressible decaying homogeneous isotropic turbulence, incompressible high-Reynolds number flat plate turbulent flow, incompressible turbulence around NACA0012 airfoil, transonic turbulence around RAE2822 airfoil, and transonic high-Reynolds number ARA M100 wing-body turbulence, are tested. The IHGKS shows the higher accuracy in space and time than that of the second-order IGKS, especially for smooth flows, and obtains more accurate turbulent flow fields on coarse grids. Compared with the explicit HGKS, the IHGKS provides great improvement on the computational efficiency. In addition, the robustness of current IHGKS and the ability to capture shock are validated in the transonic two-dimensional and three-dimensional complex RANS simulation. Transonic cases indicate that turbulence model plays a leading role in the capturing of turbulent flow in the shock-boundary interaction. Compared with numerical discretization errors, developing appropriate turbulence model is still the most important task for complex turbulence simulation.

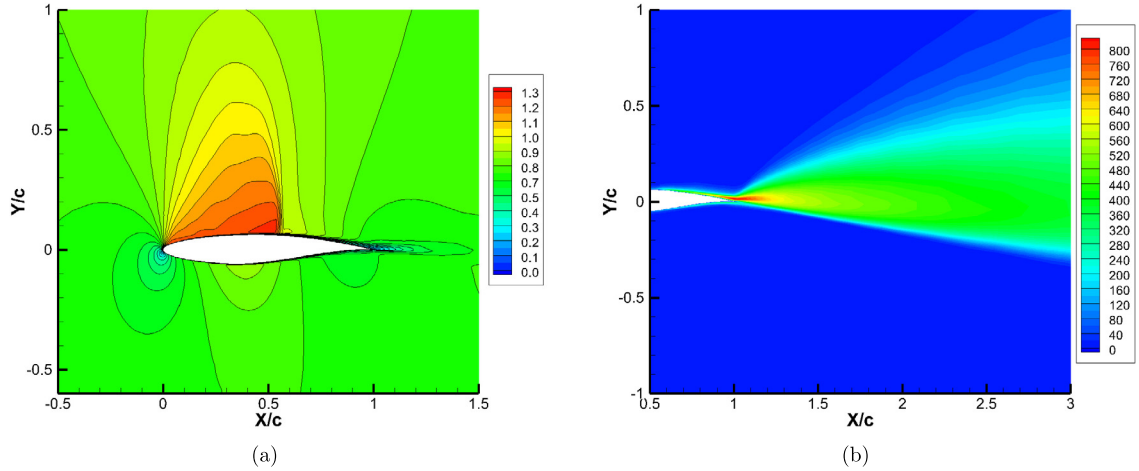

Fig. 9. Contours of Mach number (a) and normalized viscosity μ_t/μ (b) from the IHGKS on moderate grid G5 around RAE2822 airfoil. c is the chord length.

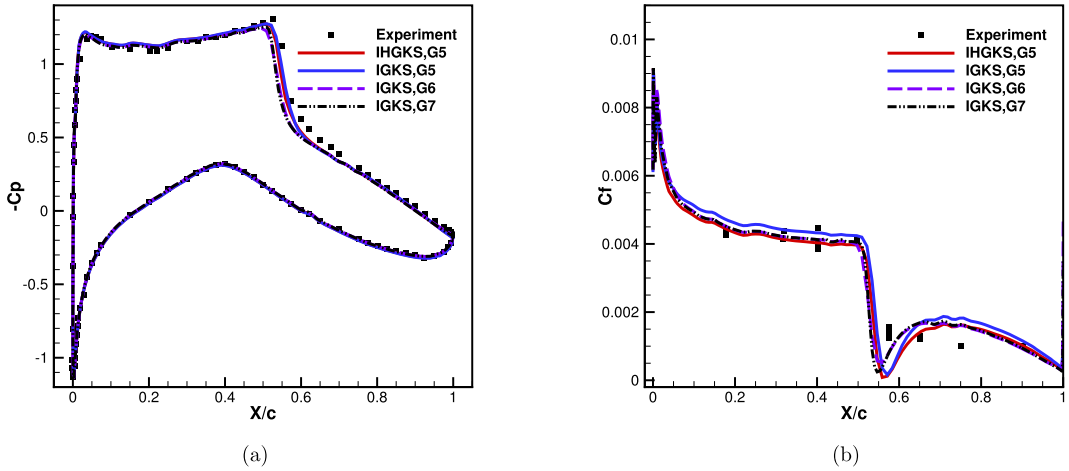

Fig. 10. Pressure coefficient distributions Cp around airfoil (a) and skin friction coefficient distributions C_f on upper airfoil (b) from the experiment data, current IHGKS, and the second-order IGKS.

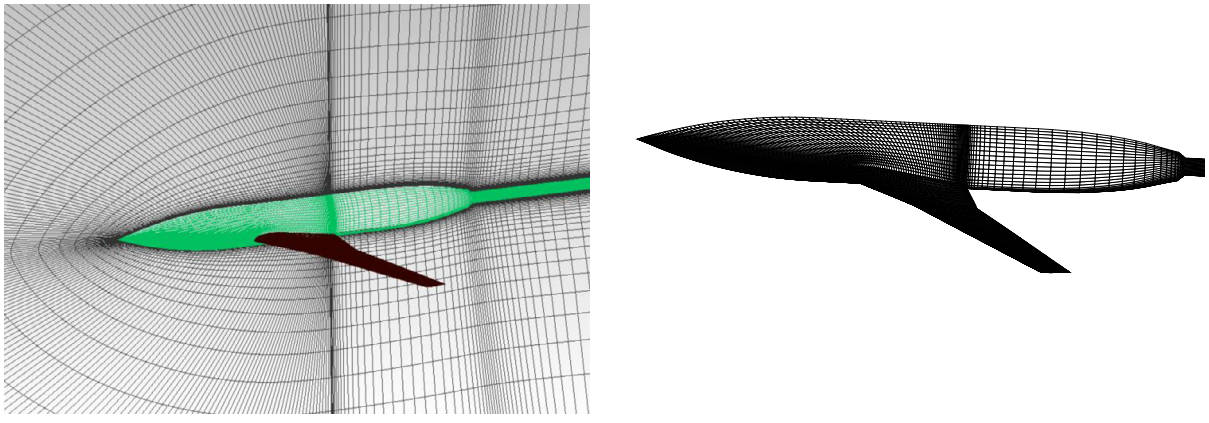

Fig. 11. Configuration of ARA M100 wing-body (a) and illustration of surface grid (b).

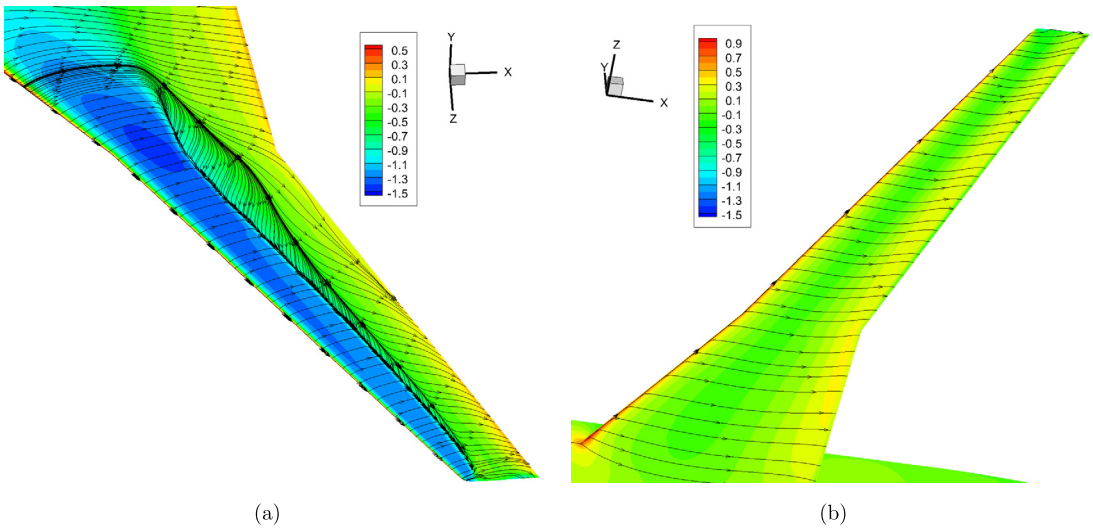

Fig. 12. Streamlines on the upper wing surface (a) and lower wing surface (b) of ARA M100 wing-body with pressure coefficient contours.

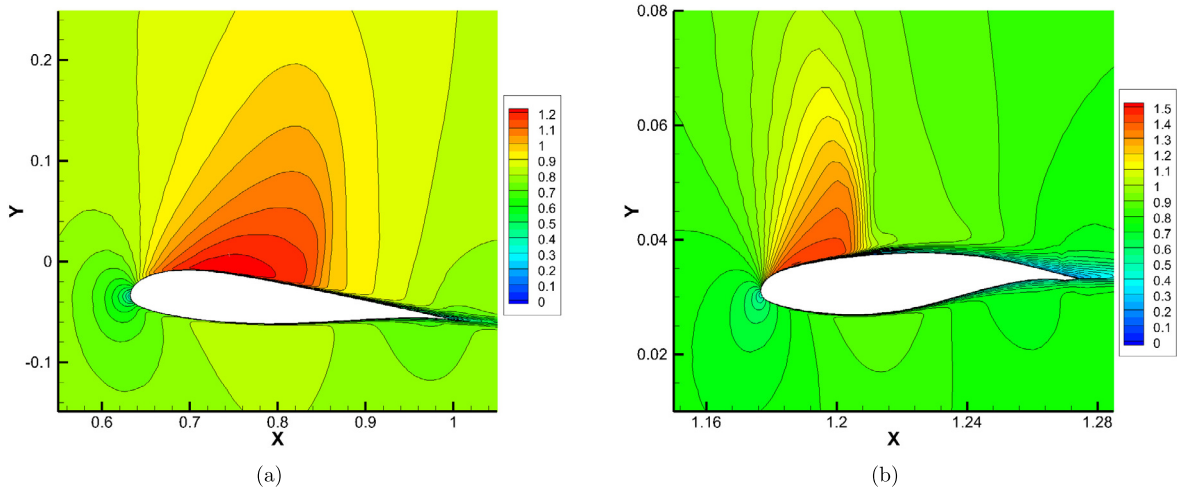

Fig. 13. Contours of Mach number at slice $Z/b = 0.019$ (a) and slice $Z/b = 0.935$ (b). Z is the distance to the root chord plane and b is the wing span of ARA M100 wing-body.

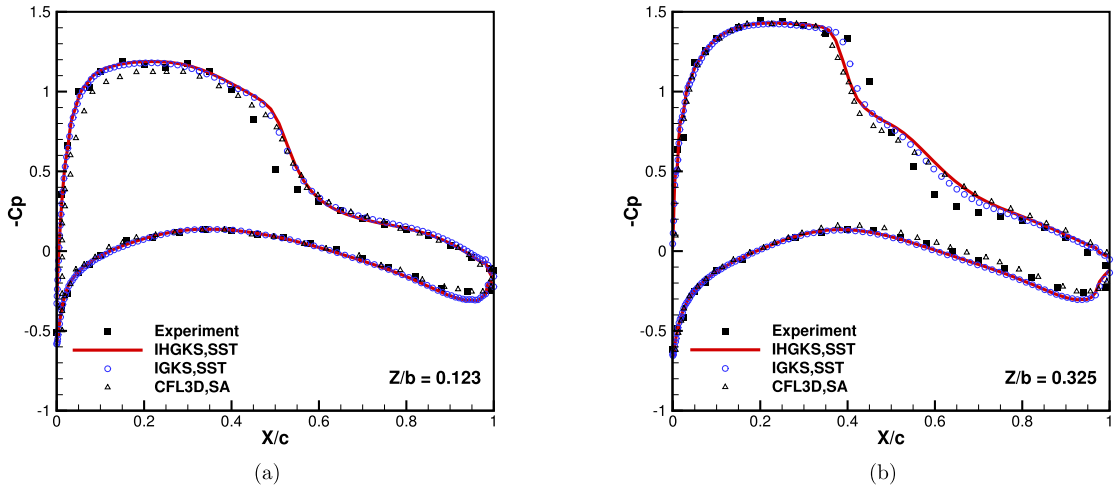

Fig. 14. Comparisons of pressure coefficient Cp profiles at selected span-wise locations of ARA M100 wing-body from the experiment data, current IHGKS, the second-order IGKS, and the second-order CFL3D. c is the local chord length.

Declaration of Competing Interest

None.

Acknowledgement

Special thanks to Shuang Tan and Hualin Liu who provide the helpful discussion and suggestions. Current research was supported by The National Key Research and Development Project of China (No. 2017YFB0202702), Hong Kong research grant council (16206617) and National Science Foundation of China (11772281, 91852114).

References

[1] Hendrik Tennekes, John Leask Lumley, A First Course in Turbulence, MIT Press, 1972.
[2] Stephen B. Pope, Turbulent Flows, 2001.
[3] John Kim, Parviz Moin, Robert Moser, Turbulence statistics in fully developed channel flow at low Reynolds number, J. Fluid Mech. 177 (1987) 133–166.
[4] Parviz Moin, Krishnan Mahesh, Direct numerical simulation: a tool in turbulence research, Annu. Rev. Fluid Mech. 30 (1) (1998) 539–578.
[5] Wei He, Peng Yu, Larry K.B. Li, Ground effects on the stability of separated flow around a NACA 4415 airfoil at low Reynolds numbers, Aerosp. Sci. Technol. 72 (2018) 63–76.
[6] Andrey Nikolaevich Kolmogorov, The local structure of turbulence in incompressible viscous fluid for very large Reynolds numbers, C. R. Acad. Sci. URSS 30 (1941) 301–305.
[7] W.P. Jones, Brian Edward Launder, The prediction of laminarization with a two-equation model of turbulence, Int. J. Heat Mass Transf. 15 (2) (1972) 301–314.
[8] David C. Wilcox, Formulation of the kw turbulence model revisited, AIAA J. 46 (11) (2008) 2823–2838.
[9] Philippe Spalart, Steven Allmaras, A one-equation turbulence model for aerodynamic flows, in: 30th Aerospace Sciences Meeting and Exhibit, 1992, p. 439.
[10] Florian R. Menter, Two-equation eddy-viscosity turbulence models for engineering applications, AIAA J. 32 (8) (1994) 1598–1605.
[11] Florian R. Menter, Martin Kuntz, Robin Langtry, Ten years of industrial experience with the SST turbulence model, Turbul. Heat Mass Transf. 4 (1) (2003) 625–632.
[12] David C. Wilcox, Turbulence Modeling for CFD, vol. 2, DCW Industries La Canada, CA, 1993.
[13] Syukuro Manabe, Joseph Smagorinsky, Robert F. Strickler, Simulated climatology of a general circulation model with a hydrologic cycle, Mon. Weather Rev. 93 (12) (1965) 769–798.
[14] Massimo Germano, Ugo Piomelli, Parviz Moin, William H. Cabot, A dynamic subgrid-scale eddy viscosity model, Phys. Fluids A, Fluid Dyn. 3 (7) (1991) 1760–1765.
[15] A.W. Vreman, An eddy-viscosity subgrid-scale model for turbulent shear flow: algebraic theory and applications, Phys. Fluids 16 (10) (2004) 3670–3681.
[16] Pierre Sagaut, Large Eddy Simulation for Incompressible Flows: An Introduction, Springer Science & Business Media, 2006.
[17] Jochen Fröhlich, Dominic Von Terzi, Hybrid LES/RANS methods for the simulation of turbulent flows, Prog. Aerosp. Sci. 44 (5) (2008) 349–377.
[18] R. Philippe Spalart, Detached-eddy simulation, Annu. Rev. Fluid Mech. 41 (2009) 181–202.
[19] Pierre Sagaut, Multiscale and Multiresolution Approaches in Turbulence: LES, DES and Hybrid RANS/LES Methods: Applications and Guidelines, World Scientific, 2013.
[20] Pietro Catalano, Marcello Amato, An evaluation of RANS turbulence modelling for aerodynamic applications, Aerosp. Sci. Technol. 7 (7) (2003) 493–509.
[21] Kun Xu, A gas-kinetic BGK scheme for the Navier–Stokes equations and its connection with artificial dissipation and Godunov method, J. Comput. Phys. 171 (1) (2001) 289–335.
[22] Kun Xu, Direct Modeling for Computational Fluid Dynamics: Construction and Application of Unified Gas-Kinetic Schemes, vol. 4, World Scientific, 2015.
[23] Prabhu Lal Bhatnagar, Eugene P. Gross, Max Krook, A model for collision processes in gases. I. Small amplitude processes in charged and neutral one-component systems, Phys. Rev. 94 (3) (1954) 511.
[24] Qibing Li, Kun Xu, Song Fu, A high-order gas-kinetic Navier–Stokes flow solver, J. Comput. Phys. 229 (19) (2010) 6715–6731.
[25] Kun Xu, Xin He, Chunpei Cai, Multiple temperature kinetic model and gas-kinetic method for hypersonic non-equilibrium flow computations, J. Comput. Phys. 227 (14) (2008) 6779–6794.
[26] Guiyu Cao, Hualin Liu, Kun Xu, Physical modeling and numerical studies of three-dimensional non-equilibrium multi-temperature flows, Phys. Fluids 30 (12) (2018) 126104.
[27] C.T. Tian, Kun Xu, K.L. Chan, L.C. Deng, A three-dimensional multidimensional gas-kinetic scheme for the Navier–Stokes equations under gravitational fields, J. Comput. Phys. 226 (2) (2007) 2003–2027.
[28] Huazhong Tang, Kun Xu, Chunpei Cai, Gas-kinetic BGK scheme for three dimensional magnetohydrodynamics, Numer. Math.: Theory Methods Appl. 3 (4) (2010) 387–404.
[29] Song Fu, Qibing Li, Numerical simulation of compressible mixing layers, Int. J. Heat Fluid Flow 27 (5) (2006) 895–901.
[30] G. Kumar, Sharath S. Girimaji, J. Kerimo, Weno-enhanced gas-kinetic scheme for direct simulations of compressible transition and turbulence, J. Comput. Phys. 234 (2013) 499–523.
[31] Hudong Chen, Satheesh Kandasamy, Steven Orszag, Rick Shock, Sauro Succi, Victor Yakhot, Extended Boltzmann kinetic equation for turbulent flows, Science 301 (5633) (2003) 633–636.
[32] Hudong Chen, Steven A. Orszag, Ilya Staroselsky, Sauro Succi, Expanded analogy between Boltzmann kinetic theory of fluids and turbulence, J. Fluid Mech. 519 (2004) 301–314.
[33] Dongxin Pan, Chengwen Zhong, Ji Li, Congshan Zhuo, A gas-kinetic scheme for the simulation of turbulent flows on unstructured meshes, Int. J. Numer. Methods Fluids 82 (11) (2016) 748–769.
[34] Jin Jiang, Yuehong Qian, Implicit gas-kinetic BGK scheme with multigrid for 3d stationary transonic high-Reynolds number flows, Comput. Fluids 66 (2012) 21–28.
[35] Marcello Righi, A gas-kinetic scheme for turbulent flow, Flow Turbul. Combust. 97 (1) (2016) 121–139.
[36] Ji Li, Chengwen Zhong, Dongxin Pan, Congshan Zhuo, A gas-kinetic scheme coupled with SST model for turbulent flows, Comput. Math. Appl. http://dx.doi.org/10.1016/j.camwa.2016.09.012.
[37] Shuang Tan, Qibing Li, Zhixiang Xiao, Song Fu, Gas kinetic scheme for turbulence simulation, Aerosp. Sci. Technol. 78 (2018) 214–227.
[38] Jiequan Li, Zhifang Du, A two-stage fourth order time-accurate discretization for Lax–Wendroff type flow solvers I. Hyperbolic conservation laws, SIAM J. Sci. Comput. 38 (5) (2016) A3046–A3069.
[39] Liang Pan, Kun Xu, Qibing Li, Jiequan Li, An efficient and accurate two-stage fourth-order gas-kinetic scheme for the Euler and Navier–Stokes equations, J. Comput. Phys. 326 (2016) 197–221.
[40] Xing Ji, Fengxiang Zhao, Wei Shyy, Kun Xu, A family of high-order gas-kinetic schemes and its comparison with Riemann solver based high-order methods, J. Comput. Phys. 356 (2018) 150–173.
[41] Seokkwan Yoon, et al., An LU-SSOR Scheme for the Euler and Navier-Stokes Equations, 1986.
[42] G. Barakos, D. Drikakis, Implicit unfactored implementation of two-equation turbulence models in compressible Navier-Stokes methods, Int. J. Numer. Methods Fluids 28 (1) (1998) 73–94.
[43] Richard Courant, Kurt Friedrichs, Hans Lewy, Über die partiellen differenzengleichungen der mathematischen physik, Math. Ann. 100 (1) (1928) 32–74.
[44] Sydney Chapman, T.G. Cowling, The Mathematical Theory of Non-Uniform Gases: An Account of the Kinetic Theory of Viscosity, Thermal Conduction and Diffusion in Gases, Cambridge Mathematical Library, vol. 1, Cambridge University Press, 1970, pp. 27–52.
[45] Taku Ohwada, Kun Xu, The kinetic scheme for the full-Burnett equations, J. Comput. Phys. 201 (1) (2004) 315–332.
[46] Guang-Shan Jiang, Chi-Wang Shu, Efficient implementation of weighted eno schemes, J. Comput. Phys. 126 (1) (1996) 202–228.
[47] Xiaodong Ren, Kun Xu, Wei Shyy, Chunwei Gu, A multi-dimensional high-order discontinuous Galerkin method based on gas kinetic theory for viscous flow computations, J. Comput. Phys. 292 (2015) 176–193.
[48] Liang Pan, Kun Xu, A third-order compact gas-kinetic scheme on unstructured meshes for compressible Navier–Stokes solutions, J. Comput. Phys. 318 (2016) 327–348.
[49] Kun Xu, Meiliang Mao, Lei Tang, A multidimensional gas-kinetic BGK scheme for hypersonic viscous flow, J. Comput. Phys. 203 (2) (2005) 405–421.
[50] Qibing Li, Song Fu, Applications of implicit BGK scheme in near-continuum flow, Int. J. Comput. Fluid Dyn. 20 (6) (2006) 453–461.
[51] Joseph Boussinesq, Essai théorique sur les lois trouvées expérimentalement par m. Bazin pour l'écoulement uniforme de l'eau dans les canaux découverts, C. R. Acad. Sci. Paris 71 (1870) 389–393.
[52] Philip L. Roe, Approximate Riemann solvers, parameter vectors, and difference schemes, J. Comput. Phys. 43 (2) (1981) 357–372.
[53] Pierre Sagaut, Claude Cambon, Homogeneous Turbulence Dynamics, vol. 10, Springer, 2008.
[54] Genevieve Comte-Bellot, Stanley Corrsin, Simple Eulerian time correlation of full-and narrow-band velocity signals in grid-generated, isotropic turbulence, J. Fluid Mech. 48 (2) (1971) 273–337.
[55] Turbulence modeling resource, https://turbmodels.larc.nasa.gov/, 2018.
[56] Nigel Gregory, C.L. O'reilly, Low-Speed Aerodynamic Characteristics of NACA 0012 Aerofoil Section, Including the Effects of Upper-Surface Roughness Simulating Hoar Frost, HM Stationery Office London, 1973.
[57] Nparc alliance verification and validation archive, https://www.grc.nasa.gov/www/wind/valid/archive.html/, 2015.

[58] P.H. Cook, M.A. McDonald, M.C.P. Firmin, Aerofoil RAE 2822: Pressure Distributions, and Boundary Layer and Wake Measurements, Experimental Data Base for Computer Program Assessment, AGARD Report ar 138, 1979.
[59] Cfl3d version 6 home page, http://cfl3d.larc.nasa.gov/, 2017.
[60] C.B. Lee, S. Fu, On the formation of the chain of ring-like vortices in a transitional boundary layer, Exp. Fluids 30 (3) (2001) 354–357.
[61] C.B. Lee, J.Z. Wu, Transition in wall-bounded flows, Appl. Mech. Rev. 61 (3) (2008) 030802.